Engineering Fracture Mechanics 343 (2026) 112253

Contents lists available at ScienceDirect

Engineering Fracture Mechanics

journal homepage: www.elsevier.com/locate/engfracmech

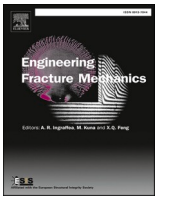

Extending GTN model to viscoplasticity for describing ductile damage in irradiated F/M steels

Roshan R. Rajakrishnan *, Ermile Gaganidze, Jarir Aktaa

Institute for Applied Materials, Karlsruhe Institute of Technology, Hermann-von-Helmholtz-Platz 1, 76344 Eggenstein-Leopoldshafen, Germany

ARTICLE INFO

Keywords:
Eurofer97
Viscoplasticity
Ductile damage
GTN
Irradiation hardening

ABSTRACT

Irradiation of Eurofer97, a reduced activation ferritic/martensitic steel used in fusion reactor applications, induces significant hardening, loss of uniform elongation (UE) and embrittlement. To estimate the maximum operating strain range of irradiated components beyond the loss of UE, a coupled deformation-ductile damage model at the component scale is proposed. This study extends the GTN ductile damage model to viscoplasticity with a simple formulation, integrating it into an existing finite strain viscoplastic model that combines kinematic hardening, isotropic softening, and irradiation hardening/softening. Therefore, the developed model captures the Bauschinger effect, finite deformation, and the irradiation-induced material changes contributing to reduction in fracture strain. Implemented in ABAQUS, the model is validated using tensile test data from both irradiated and unirradiated Eurofer97. A study on irradiation dose and initial triaxiality influence demonstrates the model's consistent and reliable predictions.

1. Introduction

Eurofer97 is a reduced activation ferritic martensitic (RAFM) steel (Fe–9Cr–1.1 W–0.2 V–0.12Ta) designed for high-radiation environments with favorable thermomechanical properties and resistance to irradiation-induced swelling [1]. It is a key structural material in the test blanket modules (TBM) of the ITER fusion reactor and is planned for use in the breeding blankets of the future DEMOnstration (DEMO) power plant. Neutron irradiation at low temperatures significantly alters Eurofer97's mechanical properties [2,3]. Dislocation pinning by irradiation defects hardens the material and increases its yield stress. Upon yielding, dislocations interact with defects either by annihilating or displacing them through channeling – a process where dislocations move along localized, defect-free paths [4,5]. This results in rapid material softening causing the ultimate-tensile-stress (UTS) to converge with the yield stress, which delivers a complete loss of uniform elongation and reduction in total elongation [6]. Interaction between dislocation and grain boundary leads to void nucleation in unirradiated and irradiated materials [7,8]. Hydrostatic stress arising from triaxial stress states drives void growth and its migration toward the necking region, where voids coalesce and cause material failure. Consequently, void nucleation, growth and coalescence is the primary damage mechanism in Eurofer97 under monotonic loading. Studies on irradiated single crystals report an accelerated void-growth and a reduction in the critical void volume fraction (VVF) for coalescence [9,10].

Current nuclear design rules [11] treat the loss of uniform elongation as a limit for certain failure modes, e.g. immediate plastic flow localization. However, this criterion is excessively conservative considering the great cost in replacing these components. Therefore, it is beneficial to identify the safe operational limits of the material in the unirradiated and irradiated states using component-scale

* Corresponding author.
E-mail address: roshan.rajakrishnan@kit.edu (R.R. Rajakrishnan).

https://doi.org/10.1016/j.engfracmech.2026.112253
Received 25 November 2025; Received in revised form 31 March 2026; Accepted 8 May 2026
Available online 9 May 2026

Nomenclature

$\boldsymbol{S}$	Cauchy stress tensor
$\boldsymbol{A}$	Almansi strain tensor
$\boldsymbol{\Sigma}$	Over-stress tensor
$\boldsymbol{I}$	Identity tensor
$\boldsymbol{D}$	Deformation rate tensor
$\boldsymbol{Z}$	Kinematic hardening tensor
$\boldsymbol{N}$	Normal tensor
$\mathbb{C}$	Elasticity tensor
ψ	Isotropic softening variable $(=\psi_1+\psi_2)$
σ_H	Irradiation hardening
Φ	GTN yield condition
f	Void volume fraction (VVF)
f^*	Effective void volume fraction
f_N	Void nucleation parameter
$\in_M$	Accumulated inelastic strain in the matrix
S_N	Standard deviation
$\in_N$	Mean nucleation strain
q_i	GTN model parameters (q_1, q_2)
f_c	Critical void volume fraction
f_u^*	GTN model parameter
f_F	GTN model parameter
σ_s	Deviatoric yield stress
σ_A	Hydrostatic yield stress
$\dot{\lambda}$	Plastic multiplier
σ_{vis}	Viscous stress
k	Initial yield stress
K	Viscous parameter
n	Viscous parameter
H	Kinematic hardening parameter
Q	Kinematic hardening parameter
R	Kinematic hardening parameter
m	Kinematic hardening parameter
ψ_s	Increase of the cyclic softening capacity
h	Isotropic softening parameter
c	Isotropic softening parameter
m_ψ	Isotropic softening parameter
ψ_r	Isotropic softening parameter
$\psi_{s,\infty}$	Isotropic softening parameter
c_s	Isotropic softening parameter
N_s	Saturation value of N
N_l	Defect available for removal
a	Defect nucleation parameter
b	Defect removal parameter
r_N	Defect removal parameter
q_N	Defect removal parameter
l_N	Stabilization threshold for defect removal
N_e	Defect removal parameter
h_N	Defect hardening coefficient
T	Temperature
σ_{eng}	Engineering stress
$\in_{eng}$	Engineering strain
σ_{true}	Mean true stress
$\in_{true}$	Mean true strain
$(\,)_{eq}$	Equivalent of tensor
$(\,)^D$	Deviatoric part of tensor
$(\,)_v$	Hydrostatic part of tensor
$(\,)_e$	Elastic part of tensor
$(\,)_p$	Plastic part of tensor

modelling. However, existing constitutive models for Eurofer97 are insufficient. Various authors have developed elastoplastic ductile damage models [12] based on Gurson-Tvergaard-Needleman (GTN) [13,14] to model Eurofer97 in its unirradiated state and at low doses [15]. These models are largely limited to monotonic loading, dose-specific calibrations, limiting their applicability to the complex working conditions of reactor components. They are not formulated for cyclic loading and do not account for irradiation-dose-dependent changes in material hardening, strain-rate sensitivity, or failure behavior. While viscoplastic GTN extensions exist to address micro-inertial effects, they generally rely on Perzyna-type approaches [16,17] which lack predictive capability at very high strain rates, or consistency approaches [18,19] which typically require complex implicit integration schemes and have only been applied to monotonic loading.

To address these limitations, this work proposes a viscoplastic extension of the rate-independent GTN formulation by Klingbeil [20], which incorporates kinematic hardening. Our approach employs a consistency-based approach, utilizing a local scalar root-finding algorithm that enforces the consistency condition by iteratively solving for the rate-dependent flow stress. This method enables robust explicit integration, retaining the accuracy of consistency-based formulations without the complex iterative return mapping algorithms typically required. The constitutive equations for kinematic hardening, isotropic softening, and irradiation-induced hardening are adopted from a finite strain viscoplastic model previously validated for cyclic loading at small strains [21] and monotonic loading at finite strains [22]. Building on these, a modified defect density evolution law to extend applicability to the high-dose range (0–70 dpa) relevant for DEMO has been added. The resulting coupled deformation-damage model, calibrated using simple load–displacement data, provides component designers with a valuable tool to investigate the feasibility of relaxing current design criteria.

The paper is organized as follows: Section 2 presents the viscoplastic extension of the GTN model of an existing model and the hardening laws used. Section 3 discusses the explicit integration algorithm used for the model and section 4 describes the model's calibration using tensile tests of unirradiated and irradiated materials. The simulation results are presented in section 5, where the influence of irradiation dose and triaxiality on the predicted material ductility is also studied. Section 6 discusses the simulation results, and section 7 concludes.

2. Constitutive model

The constitutive framework of the proposed viscoplastic damage model incorporating rate-dependence into a GTN-type model applicable to cyclic loads is introduced in this section.

2.1. Kinematics at finite strains

The finite strain framework is adopted, while elastic strains are assumed to remain small. Therefore, the Euler-Almansi strain tensor $\boldsymbol{A}$ is decomposed into elastic and plastic components [23,24],

$$\boldsymbol{A} = \boldsymbol{A}_{\mathrm{e}} + \boldsymbol{A}_{\mathrm{p}}. \tag{2.1}$$

The Oldroyd objective time derivative of $\boldsymbol{A}$ is equal to the deformation rate tensor $\boldsymbol{D}$ [24,25], such that $\overset{\Delta}{\boldsymbol{A}} = \overset{\Delta}{\boldsymbol{A}}_{\mathrm{e}} + \overset{\Delta}{\boldsymbol{A}}_{\mathrm{p}} = \boldsymbol{D}$. Oldroyd derivatives are used for tensors throughout this work to ensure frame-indifference. Subsequently, the decomposition of $\boldsymbol{D}$ leads to

$$\boldsymbol{D} = \boldsymbol{D}_{\mathrm{e}} + \boldsymbol{D}_{\mathrm{p}}. \tag{2.2}$$

The Cauchy stress tensor $\boldsymbol{S}$ is the work-conjugate to $\boldsymbol{D}$ and decomposed into deviatoric $\boldsymbol{S}^D$ and hydrostatic S_v parts through $\boldsymbol{S} = \boldsymbol{S}^D + S_v \boldsymbol{I}$, where $\boldsymbol{I}$ is the second order identity tensor. The material's elastic response is described by a Hookean hyper-elasticity equation $\boldsymbol{S} = \mathbb{C} : \boldsymbol{A}_e$. Stress evolution is given by the Oldroyd time derivative

$$\overset{\nabla}{\boldsymbol{S}} = \frac{\partial \mathbb{C}}{\partial T}\dot{T} : \boldsymbol{A}_e + \mathbb{C} : \left[\boldsymbol{D} - \boldsymbol{D}_p\right], \tag{2.3}$$

where $\mathbb{C}$ is the fourth order elasticity tensor and T is the temperature. For the isothermal process, the first term on the right side reduces to zero.

2.2. Viscoplastic framework for GTN ductile damage model

Ductile damage in metals is governed by nucleation, growth, and coalescence of voids. Void nucleation is attributed to decohesion or fracture of inclusions in the matrix material while voids growth and coalescence are driven by plastic deformation and stress triaxiality. Coalescence accelerates the damage mechanism, leading to macroscopic crack formation and finally failure. From a micromechanical perspective, it is the formation of a spherical or elliptic hole in a plastic medium that is subjected to enormous strains. Continuum Damage Mechanics describes these micromechanical processes as a reduction of the effective area resisting deformation in any plane of a Representative Volume Element (RVE).

Ductile damage in porous metals is commonly described using the rate-independent Gurson–Tvergaard–Needleman (GTN) framework [26,27], where the influence of voids on yielding is represented through the void volume fraction f. To describe strain hardening of the material under cyclic or non-monotonic loading, an extension of the GTN model was proposed by Klingbeil [20] based

on unit cell simulations, which demonstrated that kinematic hardening influences strain localization on a mesoscopic scale and therefore the damage development. The extended GTN yield function is given by

$$\Phi = \left(\frac{\Sigma_{eq}}{\sigma_S}\right)^2 + 2f^* q_1 \, Cosh\left(\frac{3\,q_2\,\Sigma_v}{2\,\sigma_A}\right) - 1 - (q_1 f^*)^2 = 0 \tag{2.4}$$

where Σ_{eq} is the von Mises equivalent of the over-stress tensor $\boldsymbol{\Sigma} = \boldsymbol{S} - (1 - q_1 f^*)\boldsymbol{Z}$. Here, $\boldsymbol{\Sigma}$ incorporates the kinematic hardening variable ($\boldsymbol{Z}$), following Mear and Hutchinson [28], to account for yield surface translation and the Cauchy stress tensor $\boldsymbol{S}$. The hydrostatic component satisfies $\Sigma_v \approx S_v$, since $S_v \gg Z_v$. Parameters σ_S and σ_A are tensile flow stresses associated with the deviatoric and hydrostatic parts of the yield function respectively, introduced to address distinct hardening mechanisms [29,30]. As the matrix alone undergoes kinematic hardening [20,28], the history dependent σ_A was introduced to track the material hardening and therefore determines the so-called limiting surface. Parameters q_1 and q_2 were introduced to account for void interaction effects [13,27]. The eq. (2.4) reduces to the original GTN model for $\boldsymbol{\Sigma} = \boldsymbol{S}$ and $\sigma_A = \sigma_S$. To capture the rapid material degradation associated with void coalescence, the effective void volume fraction f^* is defined as a piecewise function of the current void volume fraction f and the critical value f_c at which coalescence initiates:

$$f^* = \begin{cases} f & , if\ f \le f_c \\ f_c + \dfrac{f_u^* - f_c}{f_F - f_c}(f - f_c) & , if\ f > f_c. \end{cases} \tag{2.5}$$

where f_F denotes the value of f at final fracture and f_u^* is the corresponding upper bound of f^*, typically taken as $f_u^* = 1/q_1$.

Existing viscoplastic GTN formulations commonly employ a consistency-based formulation with a rate-dependent yield surface, maintaining the Kuhn–Tucker loading–unloading conditions [18,19]. Rate effects are typically introduced through the matrix strain using Norton-type laws, which complicates the inclusion of kinematic hardening and requires implicit integration [31]. Explicit integration of GTN models is challenging due to the strong nonlinearity of the yield function, the evolution of f becomes highly sensitive near coalescence, and the difficulty of ensuring the consistency condition ($\Phi = 0$) within explicit schemes.

In this work, a viscoplastic extension of the Klingbeil model is proposed to overcome these limitations. The viscous effect of the RVE is exclusively associated with the matrix material and is therefore assumed to be driven by the deviatoric stress alone. The viscoplastic consistency condition $\Phi \ge 0$ is applied to eq. (2.4). The stress states fulfilling this condition lie outside the yield surface by a magnitude defined as the viscous stress (σ_{vis}). Therefore, the inequality is modified by updating the yield stress with the addition of σ_{vis}, resulting in the following equality which satisfies the Kuhn-Tucker conditions, and describes all stress states with the same σ_{vis} and thus the viscoplastic potential

$$\Phi = \left(\frac{\Sigma_{eq}}{\sigma_S + \sigma_{vis}}\right)^2 + 2f^* q_1 \, Cosh\left(\frac{3\,q_2\,\Sigma_v}{2\,(\sigma_A + \sigma_{vis})}\right) - 1 - (q_3\, f^*)^2 = 0. \tag{2.6}$$

The GTN yield and potential surfaces are illustrated in Fig. 1. For a given stress state fulfilling $\Phi \ge 0$, σ_{vis} is determined by solving eq.

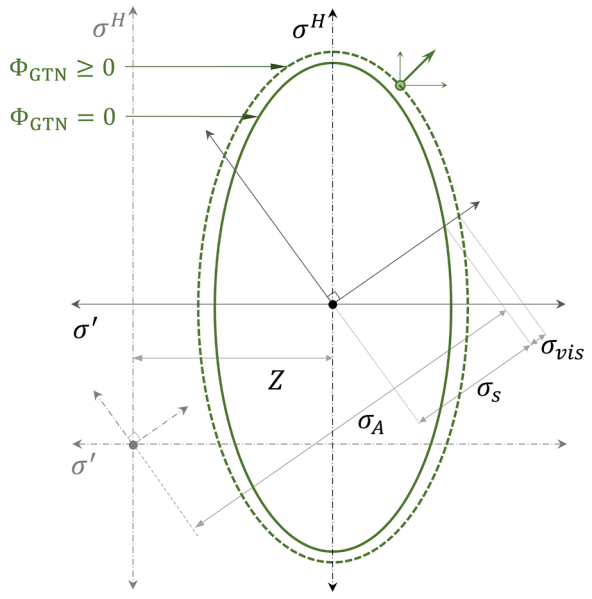

Fig. 1. Viscoplastic GTN yield potential with kinematic hardening.

(2.6). σ_{vis} introduces a strain-rate dependence to the matrix flow stress, accounting for the material's intrinsic strain-rate sensitivity [32,33]. This allows the determination of the accumulated inelastic strain rate in the matrix from the power law

$$\dot{\epsilon}_m = \left\langle \frac{\sigma_{vis}}{K} \right\rangle^n . \tag{2.7}$$

Here n and K are viscous parameters that control the rate-sensitivity and the magnitude of viscous flow resistance, respectively.

The limiting surface given by σ_A is proposed to be

$$\sigma_A = \max_{-\infty<\tau<t} \sigma_S(\tau) + \max_{-\infty<\tau<t} Z_{eq}(\tau)\,, \tag{2.8}$$

which corresponds to the farthest stress state achieved by the yield surface during the load history.

The inelastic strain rate is got by applying the normality rule on the viscoplastic potential in eq. (2.6)

$$\boldsymbol{D}_p = \dot{\lambda}\frac{\partial \Phi}{\partial \boldsymbol{\Sigma}} = \dot{\lambda}\boldsymbol{N}, \tag{2.9}$$

where $\dot{\lambda}$ is the viscoplastic multiplier and $\boldsymbol{N}$ is the normal tensor to the potential surface

$$\boldsymbol{N} = \frac{\partial \Phi}{\partial \Sigma_v}\frac{\partial \Sigma_v}{\partial \boldsymbol{\Sigma}} + \frac{\partial \Phi}{\partial \Sigma_{eq}}\frac{\partial \Phi_{eq}}{\partial \boldsymbol{\Sigma}} = \frac{f^* q_1 q_2}{\sigma_A + \sigma_{vis}} Sinh\left(\frac{3}{2} q_2 \frac{\Sigma_v}{\sigma_A + \sigma_{vis}}\right)\boldsymbol{I} + \frac{3\boldsymbol{\Sigma}^D}{(\sigma_S + \sigma_{vis})^2}\,. \tag{2.10}$$

Here, the first and the second terms are related to hydrostatic and deviatoric stress, respectively. As the power dissipated by the inelastic deformation of the considered damaged volume element originates from the matrix [27,34,35], the following is derived

$$\boldsymbol{\Sigma} : \boldsymbol{D}_p = (1-f)(\sigma_S + \sigma_{vis})\,\dot{\epsilon}_m. \tag{2.11}$$

The viscoplastic multiplier $\dot{\lambda}$ is identified by substituting the equations (2.7), (2.9) and (2.10) into eq. (2.11)

$$\dot{\lambda} = (1-f)\frac{\sigma_S + \sigma_{vis}}{\boldsymbol{\Sigma} : \boldsymbol{N}} \left\langle \frac{\sigma_{vis}}{K} \right\rangle^n. \tag{2.12}$$

Here,

$$\boldsymbol{\Sigma} : \boldsymbol{N} = \frac{2\Sigma_{eq}^2}{(\sigma_s + \sigma_{vis})^2} + \Sigma_v \frac{f^* q_1 q_2}{\sigma_A + \sigma_{vis}} Sinh\left(\frac{3}{2} q_2 \frac{\Sigma_v}{\sigma_A + \sigma_{vis}}\right). \tag{2.13}$$

Therefore, the inelastic strain rate from eq. (2.9) becomes

$$\boldsymbol{D}_p = (1-f)\left\langle \frac{\sigma_{vis}}{K} \right\rangle^n \frac{\sigma_S + \sigma_{vis}}{\boldsymbol{\Sigma} : \boldsymbol{N}} \left[\frac{f^* q_1 q_2}{\sigma_A + \sigma_{vis}} Sinh\left(\frac{3}{2} q_2 \frac{\Sigma_v}{\sigma_A + \sigma_{vis}}\right)\boldsymbol{I} + \frac{3\boldsymbol{\Sigma}^D}{(\sigma_S + \sigma_{vis})^2}\right]. \tag{2.14}$$

2.3. Hardening laws for irradiated material

In this work, several hardening laws from [22,36] are adopted. Therefore, the over-stress tensor is defined as

$$\boldsymbol{\Sigma} = \frac{\boldsymbol{S}}{\psi} - \boldsymbol{Z}, \tag{2.15}$$

where ψ is the dimensionless isotropic softening variable. The kinematic hardening variable $\boldsymbol{Z}$ is given by the summation of multiple variables $\boldsymbol{Z}_i$ which follow the Chaboche non-linear hardening rule [37]

$$\boldsymbol{Z} = \sum_i^{m_Z} \boldsymbol{Z}_i \quad \text{and} \quad \overset{\nabla}{\boldsymbol{Z}}_i = H_i \boldsymbol{D}_p^D - Q_i \dot{p}\boldsymbol{Z}_i + R\,|\boldsymbol{Z}_i|^{m-1}\boldsymbol{Z}_i \tag{2.16}$$

where $\boldsymbol{D}_p^D$ is used to ensure the deviatoric nature of the kinematic hardening $\boldsymbol{Z}$. Here, three variables are used (i.e., $m_Z = 3$). The accumulated plastic strain rate is

$$\dot{p} = \sqrt{\frac{2}{3}\boldsymbol{D}_p : \boldsymbol{D}_p}. \tag{2.17}$$

The isotropic softening variable ψ is given by the evolution of two sub-variables [36]

$$\dot{\psi}_1 = -h\dot{p}\,, \quad \dot{\psi}_2 = c(\psi_s - \psi_2)\dot{p} - r_\psi|\psi_2 - \psi_r|^{m_\psi - 1}(\psi_2 - \psi_r). \tag{2.18}$$

Here, $\psi_s = 1 - \psi_{s,\infty}\left(1 - exp\left(-c_s\,\varepsilon_{eq,\,max}^{in}\right)\right)$ describes the increase of the cyclic softening capacity corresponding to $\varepsilon_{eq,\,max}^{in}$, the

highest value of the von Mises strain equivalent of $\boldsymbol{D}_p$ during the load history. Parameters c, m_ψ, ψ_r, ψ_s, and c_s are temperature and material dependent.

Strain hardening in Eurofer97 is independent of irradiation [38]. Irradiation-influenced changes in material behavior are modelled using a defect density variable N [36] for 'i' type of defects

$$\dot{N}_i(\phi, p) = a_i\left(N_{s,i} - N_i\right)\dot{\phi} - b_i\left(N_i - N_{l,i}\right)\dot{p} - r_{N,i}N^{q_{N,i}}. \tag{2.19}$$

The first term describes defect formation due to irradiation dose, ϕ saturating at $N_{s,i}$. The second term describes the defect removal controlled by $N_{l,i}$. Healing of defects at high temperatures is given by the last term. Parameters a_i, b_i, $r_{N,i}$, $q_{N,i}$, $N_{s,i}$ are material and temperature dependent. The deformation driven $N_{l,i}$ is based on [22]

$$N_{l,i} = \left\langle \sqrt{N_i(\tau)} \cdot \left(1 - l_{N,i}\left(2 - e^{-N_e p}\right)\right)\right\rangle^2. \tag{2.20}$$

where, $l_{N,i}$ and N_e are dimensionless, temperature and material-dependent parameters. l_N represents the fraction of irradiation-induced defects that can be removed before the defect removal rate stabilizes and subsequently proceeds at a rate controlled by N_e. As l_N is observed to decrease with increase in σ_H, it is defined in this work as a function of $\sigma_{H,\,max} = \max_{-\infty<\tau<t} \sigma_H(\tau)$. Therefore, l_N is linearly interpolated between its extremal values $l_{N,1}$ and $l_{N,0}$ with respect to $\sigma_{H,\,max}$. Here, $l_{N,1}$ corresponds to the saturation associated with $\sqrt{N_s}$ at higher irradiation doses and $l_{N,0}$ is obtained by extrapolation to $\sigma_H = 0$ MPa for unirradiated material, serving as a modelling parameter without direct physical significance. The quadratic $\sigma_H - \phi$ relationship produces an artificially high saturation threshold ($l_N \cdot \sigma_{H,max}$) at intermediates doses for $T_{test} = 300\ ^\circ$C (Fig. 2). This anomaly disappears when an exponential fit is used, indicating that introducing a non-linear l_N-$\sigma_{H,\,max}$ relationship is likely and presents a potential improvement to the model.

Irradiation hardening σ_H for n_H defect types is calculated using the relation

$$\sigma_H = \sum_i^{n_H} \sigma_{H,i} \text{ with } \sigma_{H,i} = \sqrt{h_{N,i}^2 N_i}. \tag{2.21}$$

Here, h_N is a temperature and material dependent parameter that includes the temperature influence on the hardening contributed by the irradiation defects. Therefore, for an irradiated material $\sigma_s = \sigma_H + k$, with k denoting the initial temperature-dependent yield stress of the unirradiated material.

As irradiation reduces the strain-rate sensitivity of RAFM steels [39], the viscous parameter n_{irr} is used for the irradiated material in place of n.

2.4. Porosity evolution

Evolution of VVF is described by the summation of void nucleation and growth [26]. Assuming plastic incompressibility, void growth is described by

$$\dot{f}_{growth} = (1 - f)\,\text{trace}\left(\boldsymbol{D}_p\right). \tag{2.22}$$

Void nucleation is linked to $\in_M$ and follows a normal distribution [34] controlled by the mean nucleation strain ($\in_N$), the VVF of nucleating particles (f_N) and the standard deviation (S_N).

$$\dot{f}_{nucleation} = \frac{f_N}{s_N\sqrt{2\pi}}\, exp\left[-0.5\left(\frac{\in_M - \in_N}{s_N}\right)^2\right] \tag{2.23}$$

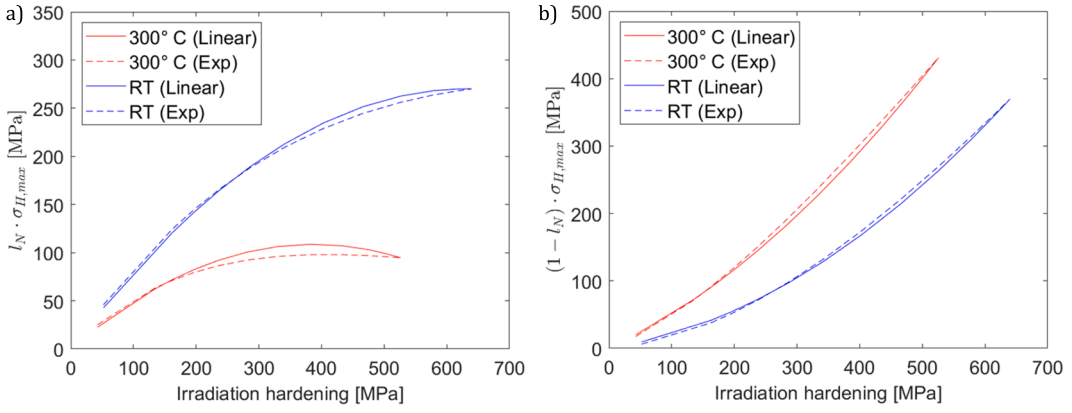

Fig. 2. Influence of l_N on hardening saturation: a) removable and b) residual contributions as functions of $\sigma_{H,max}$.

3. Corotational integration algorithm

The proposed model is implemented in the commercial FEA code Abaqus through the user subroutine, UMAT [40]. For the corotational stress $\boldsymbol{S}_0^* = \Delta\boldsymbol{R}\cdot\boldsymbol{S}_0\cdot\Delta\boldsymbol{R}^T$ provided at beginning of time increment t_0 and corotational strain increment $\Delta\boldsymbol{\in}$, an update to stress is expected at the end of the increment, t_1. Here, $\boldsymbol{S}_0$ is the Cauchy stress at t_0 and $\Delta\boldsymbol{R}$ is the rotation increment. $\Delta\boldsymbol{R}$ and $\Delta\boldsymbol{\in}$ are defined by Abaqus following Hughes and Winget [41]. For a corotational rotation tenor $\boldsymbol{Q}(\zeta)$, $\zeta\in[t_0,\ t_1]$ such that $\boldsymbol{Q}(t_0)=\boldsymbol{I}$ and $\boldsymbol{Q}(t_1)=\Delta\boldsymbol{R}$, Weber [42] introduced the bar-transformation of stress in the corotational frame

$$\overline{\boldsymbol{S}}(\zeta)=\boldsymbol{Q}^T(\zeta)\cdot\boldsymbol{S}(\zeta)\cdot\boldsymbol{Q}(\zeta) \tag{3.1}$$

and showed that the time derivative of $\overline{\boldsymbol{S}}$ is related to the Jaumann derivative through

$$\dot{\overline{\boldsymbol{S}}}(\zeta)=\boldsymbol{Q}^T(\zeta)\cdot\overset{\circ}{\boldsymbol{S}}(\zeta)\cdot\boldsymbol{Q}(\zeta). \tag{3.2}$$

With rigid-body rotation eliminated, the objective stress rate reduces to a simple time derivative in the corotational frame. The updated stress, obtained from implicit integration of the evolution equations, is subsequently rotated back to the current configuration. An explicit integration based on this approach was proposed by Jansohn [23], implemented in [22], and is adopted again in the present work.

Oldroyd derivatives from Eqs. (2.3) and (2.16) are reformulated in terms of Jaumann rate, and bar-transformed as:

$$\dot{\overline{\boldsymbol{S}}}=\boldsymbol{Q}^T\cdot\overset{\circ}{\boldsymbol{S}}\cdot\boldsymbol{Q}=\overline{\boldsymbol{D}}\cdot\overline{\boldsymbol{S}}+\overline{\boldsymbol{S}}\cdot\overline{\boldsymbol{D}}+\mathbb{C}:\left[\overline{\boldsymbol{D}}-\overline{\boldsymbol{D}}_p\right] \tag{3.3}$$

$$\dot{\overline{\boldsymbol{Z}}}_i=\boldsymbol{Q}^T\cdot\overset{\circ}{\boldsymbol{Z}}_i\cdot\boldsymbol{Q}=\overline{\boldsymbol{D}}\cdot\overline{\boldsymbol{Z}}_i+\overline{\boldsymbol{Z}}_i\cdot\overline{\boldsymbol{D}}+H_i\overline{\boldsymbol{D}}_p^D-Q_i\dot{p}\,\overline{\boldsymbol{Z}}_i+R\,|\overline{\boldsymbol{Z}}_i|^{m-1}\overline{\boldsymbol{Z}}_i. \tag{3.4}$$

Let $y=[\boldsymbol{S},\ p,\ \in_M,\ \boldsymbol{Z}_i,\ \psi,\ N,\ f]$ denote the vector of state variables, with $\dot{y}$ and y_0 representing their time derivatives and the initial values. For isothermal conditions, the numerical integration proceeds as follows:

1. Transform stress tensor to the corotational frame at t_0

$$\overline{\boldsymbol{S}}_0=\boldsymbol{Q}^T\cdot\boldsymbol{S}_0^*\cdot\boldsymbol{Q} \tag{3.5}$$

2. Initialize $y_0=\left[\overline{\boldsymbol{S}}_0,\ p_0,\ \in_{M,0},\ \overline{\boldsymbol{Z}}_{i,0},\ \psi_{i,0},\ N_0,\ f_0\right]$ using values from the previous time step. At $t_0=0$, $y_0=0$ except $\psi_{2,0}=1$.
3. Obtain $\overline{\Delta\boldsymbol{\in}}$ from the transformation $\overline{\Delta\boldsymbol{\in}}=\boldsymbol{Q}^T\cdot\Delta\boldsymbol{\in}\cdot\boldsymbol{Q}$ and compute the rate of deformation $\overline{\boldsymbol{D}}=\overline{\Delta\boldsymbol{\in}}/\Delta t$. Irradiation dose rate $\dot{\phi}$ is provided through the user-field subroutine USDFLD.
4. Temperature-dependent model parameters are interpolated and the trial stress using is computed as

$$\overline{\boldsymbol{S}}_{1,\,trial}=\overline{\boldsymbol{S}}_0+\mathbb{C}:\overline{\Delta\boldsymbol{\in}}. \tag{3.6}$$

5. Defect density N is integrated using an explicit Runge-Kutta-Fehlberg (RKF) scheme [43]

$$\dot{N}=a(N_s-N)\dot{\phi},\ \ \sigma_H=h_N\sqrt{N}. \tag{3.7}$$

6. The yield criterion from eq. (2.6) is evaluated.

Elastic step: If yield function is not satisfied, trial stress is accepted as final stress $\left(\overline{\boldsymbol{S}}_1=\overline{\boldsymbol{S}}_{1,\,trial}\right)$ and the initial values of state variables remain unchanged. The elastic tensor is adopted as the consistent tangent modulus, $\overline{\mathbb{C}}_{CTM}$.

Inelastic step: If yield condition is satisfied:

i. The coupled constitutive equations are integrated using the RKF scheme. The integration initializes with y_0 to solve for updated values of $\overline{\boldsymbol{S}}_1$, $\overline{\boldsymbol{Z}}_{i,1}$, p_1, $\in_{M,1}$, $\psi_{i,1}$, N_1 and f_1. During integration, σ_{vis} is determined through the BRENT algorithm [44] to ensure robustness during void coalescence.

ii. The consistent tangent modulus $\overline{\mathbb{C}}_{CTM}$ is approximated numerically following Fleig [45] and the inelastic strain tensor is updated using Eqs. (2.7) and (2.14), to determine $\varepsilon^{in}_{eq,\,max}$.

7. The updated tensorial variables are rotated to the current configuration

$$\boldsymbol{S}_1=\boldsymbol{Q}\cdot\overline{\boldsymbol{S}}_1\cdot\boldsymbol{Q}^T,\ \ \boldsymbol{Z}_{i,1}=\boldsymbol{Q}\cdot\overline{\boldsymbol{Z}}_{i,1}\cdot\boldsymbol{Q}^T,\ \ \boldsymbol{A}_{p,1}=\boldsymbol{Q}\cdot\overline{\boldsymbol{A}}_{p,1}\cdot\boldsymbol{Q}^T. \tag{3.8}$$

8. The $\overline{\mathbb{C}}_{CTM}$ is rotated to current configuration following a simplified approach as an orientation in line with the $\boldsymbol{S}_1$ is reported to aid global convergence [46,47]

$$\mathbb{C}_{CTM} = (\boldsymbol{Q} \otimes \boldsymbol{Q}) : \overline{\mathbb{C}}_{CTM} : (\boldsymbol{Q}^T \otimes \boldsymbol{Q}^T), \text{ i.e. } (\mathbb{C}_{CTM})_{ijkl} = \boldsymbol{Q}_{im}\boldsymbol{Q}_{jn}\boldsymbol{Q}_{kp}\boldsymbol{Q}_{lq}(\overline{\mathbb{C}}_{CTM})_{mnpq} \quad 3.9$$

Here, $\boldsymbol{Q} \otimes \boldsymbol{Q}$ denotes the fourth-order tensor defined by $(\boldsymbol{Q} \otimes \boldsymbol{Q})_{ijkl} = \boldsymbol{Q}_{ik}\boldsymbol{Q}_{jl}$. The isotropic elastic tensor $\mathbb{C}$ used in elastic step doesn't require to be rotated and remains unaffected by rotation. Therefore, the material routine uniformly rotates $\overline{\mathbb{C}}_{CTM}$ regardless of elastic or inelastic deformation.

9. The updated stress $\boldsymbol{S}_1$, tangent modulus $\mathbb{C}_{CTM}$, and all internal state variables are returned to Abaqus
10. The overall numerical procedure is summarized in the flowchart shown in Fig. 3. Using this UMAT implementation, the model is calibrated using experimental tensile test results.

4. Model calibration

The model is calibrated using camera-monitored tensile tests performed at SCK-CEN [48] within the M4F project (European Horizon2020) on unirradiated and irradiated ($T_{irr} = 300$ °C) Eurofer97 specimens [22] at RT and 300 °C, with a gauge length of 12 mm and diameter (d_0) of 2.4 mm. Displacement rates ($\dot{u}$) of 0.2 and 2.0 mm/min on the unirradiated, and 0.2 mm/min on the irradiated specimens were chosen. The testing conditions and tensile properties of irradiated specimens, including the test temperature T_{test}, yield stress $R_{0.2}$, hardening σ_H, uniform elongation A and total elongation A_g are summarized in Table 1. Due to limited material availability, every loading condition was tested with a single specimen and all experimental data obtained at RT and 300 °C were used for parameter identification. Two unirradiated tests at 100 and 200 °C at a deformation rate of 2.0 mm/min are reserved for blind validation. True stress–strain curves ($\sigma_T - \in_T$) were obtained from optical measurements of the neck following [22].

Several model parameters are adopted from the literature and past work, and are kept fixed in the present study. The elastic constants (E, ν), kinematic hardening parameters R and m, and the isotropic softening parameters (h, c, r_ψ, ψ_r, m_ψ, $\psi_{s,\infty}$ and c_s) at RT and 300 °C are adopted from [36]. For the GTN model, the parameters q_1 and q_2 from [27], and the void-nucleation parameters $\in_N$ and s_N from [27,34] are used. The parameters f_F and the experimentally determined f_c for unirradiated Eurofer97 at RT are taken from [12]. The initial yield stress k, and the kinematic hardening parameters H_i and C_i previously reported in [22] for 300 °C are retained.

Material softening is described by isotropic softening, irradiation defect removal, and porosity evolution. The kinematic hardening parameters are identified such that the isotropic softening is compensated at large strains. Consequently, irradiation defect removal and porosity evolution primarily influence neck development and strain localization. To regulate localization and separate the contributions of individual softening mechanism during parameter identification, viscoplastic regularization is introduced through the

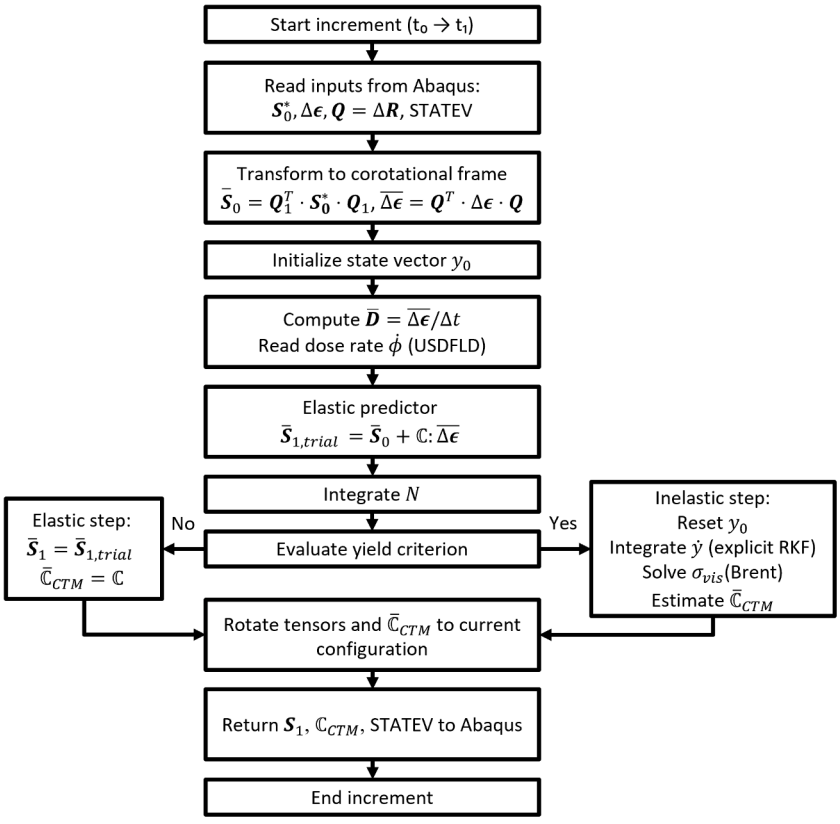

Fig. 3. Computational flowchart of the UMAT implementation showing the integration algorithm.

Table 1
Tensile properties of unirradiated and irradiated specimens tested.

T_{test} (°C)	$\dot{u}$ (mm/min)	Dose (dpa)	$R_{0.2}$ (MPa)	σ_H (MPa)	A	A_g
RT	0.2	0	641	0	5.15	20.01
RT	0.2	1.05	862	221	0.62	11.93
RT	2.0	0	649	0	5.42	20.24
100	2.0	0	571.5	0	4.08	19.65
200	2.0	0	544	0	3.94	18.61
300	2.0	0	478	0	2.97	17.08
300	0.2	0	502	0	2.6	16
300	0.2	0.65	654.7	152.7	0.67	11.2
300	0.2	1.18	744	242	0.57	10.5

viscous parameters n and n_{irr}.

From the $\sigma_T - \in_T$ data of the unirradiated material tested at 0.2 mm/min, the equivalent plastic strain (p) is extracted and used to estimate ψ. Initial estimates of k, H_i and C_i are obtained by fitting σ_T/ψ following [22],

$$\frac{\sigma_T}{\psi} = k + \sigma_{vis} + \sum_{i}^{3} \frac{H_i}{Q_i}\left(1 - e^{-Q_i p}\right) \tag{4.1}$$

assuming $\sigma_{vis} = 1$ MPa. The parameters k, n, K, H_i and C_i are then identified using an inverse multi-objective optimization procedure with engineering curves at 0.2 and 2.0 mm/min as reference data. The resulting strain hardening parameters are listed in Table 2.

The irradiation defect nucleation parameters a, $\sqrt{N_s}$ and h_N are got by fitting σ_H data from Table 1 and from literature [6,49] using the relation $\sigma_H = \sqrt{h_N^2 N_s}\,(1 - exp(-a\phi))^{0.5}$ [50]. Since defect density nucleated at $T_{irr} = 300$ °C is temperature-independent, $h_N = 1.0$ is fixed at 300 °C. The fitting results are shown in Fig. 5. The viscous parameter n_{irr}, and the defect removal parameters b, l_N and N_e are identified from load-displacement data at low and high doses (70 dpa) [22,51,52] using an optimization procedure. While n_{irr}, b and N_e are dose-independent, l_N decreases with increasing $\sigma_{H,max}$. While a non-linear fit is more suitable for $l_N - \sigma_{H,max}$ due to the quadratic $\sigma_H - \phi$ relationship, there is insufficient data. Therefore, a linear fit is used to determine the extremal values of l_N. $l_{N,1}$ relates to the $\sqrt{N_s}$, while $l_{N,0}$ is extrapolated for $\sigma_H = 0$ MPa. The irradiation defect evolution parameters are listed in Table 4.

For the unirradiated material, the GTN parameters f_N and f_F are identified together with n, while all other parameters are fixed. Void growth induces additional softening and accelerates strain localization, which is regulated by viscoplastic regularization through n, enabling the separation of isotropic and damage-induced softening during parameter identification and improving the numerical robustness. In irradiated materials, accelerated void coalescence has been reported for FCC single crystals [9] and RAFM steels [10,53]. Since an experimental determination of critical VVF for irradiated Eurofer97 is beyond the scope of the present work, $f_{c,irr}$ is treated as a fitting parameter. Similar to the unirradiated case, $f_{c,irr}$ and n_{irr} are identified simultaneously. Here again, viscoplastic regularization governed by n_{irr} allows the separation of softening from void growth and irradiation defect removal. The parameter identification process is summarized in Fig. 4.

The resulting set of parameters for irradiated condition identified from tests at 0.65, 1.05, and 1.18 dpa [22] (Table 3), is found to remain applicable up to 70 dpa [51]. However, the following relationships are noticed

$$\frac{n_{irr}@RT}{n_{irr}@300^{\circ}C} \approx \frac{f_{irr}@RT}{n_{irr}@300^{\circ}C} \approx \frac{h_N@RT}{h_N@300^{\circ}C} \text{ and } \left.\frac{f_{c,irr}}{n_{irr}}\right|_{RT} = \left.\frac{f_{c,irr}}{n_{irr}}\right|_{300\,^{\circ}C} \tag{4.2}$$

which indicate that temperature dependence of irradiated material properties is linked to h_N. As uniform elongation vanishes at approximately 0.7 dpa [54], the material is assumed to transition from the unirradiated to the fully irradiated state at this dose [54]. Due to the lack of experimental data in the 0–0.7 dpa range, the viscous parameter n and critical void volume fraction f_c are linearly interpolated between their unirradiated and their irradiated values between 0 and 0.7 dpa.

5. Numerical simulation of tensile tests

Tensile tests on unirradiated and irradiated specimens are simulated in Abaqus using the developed material model and compared with experimental data at $T_{test} = 300$ °C. An axisymmetric FE-model of the smooth tensile test specimen (Fig. 6) [22] is used. The finite strain framework is enabled using NLGEOM option. A symmetry boundary condition is applied along the x axis, and displacement is

Table 2
Parameters identified for strain hardening material laws. Parameters marked with * are taken from literature [22,36].

T (°C)	E (GPa)	ν	k (MPa)	n	K (MPa $s^{1/n}$)	H_1 (MPa)	Q_1	H_2 (MPa)	Q_2	H_3 (MPa)	Q_3
RT	208*	0.3*	424.3	10.1	117.76	139042	784.9	3814	42.8	624	0.29
300	200*	0.3*	335*	6.62	28.71	3320034*	2166*	7538.7*	125.8*	525.5*	0.58*

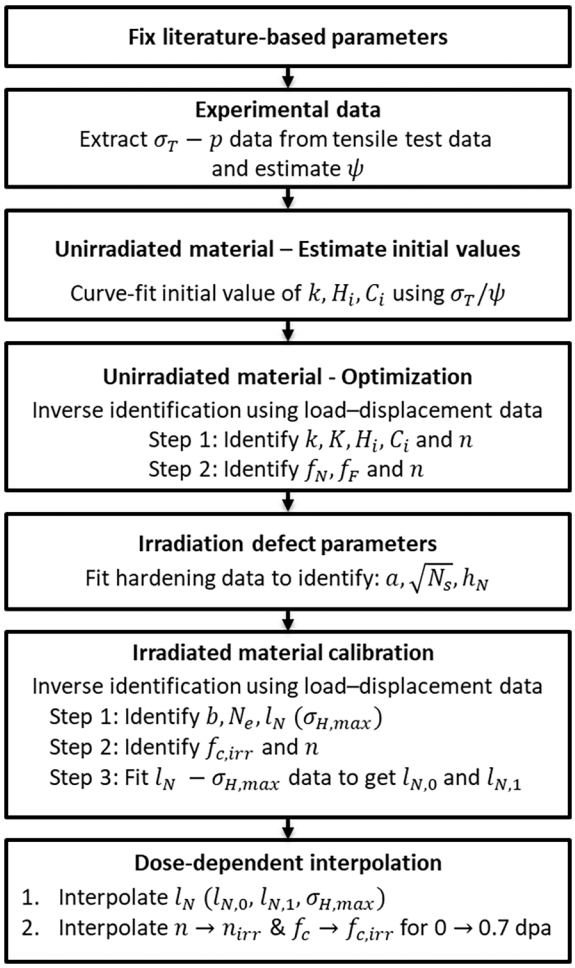

Fig. 4. Flowchart showing the parameter identification strategy.

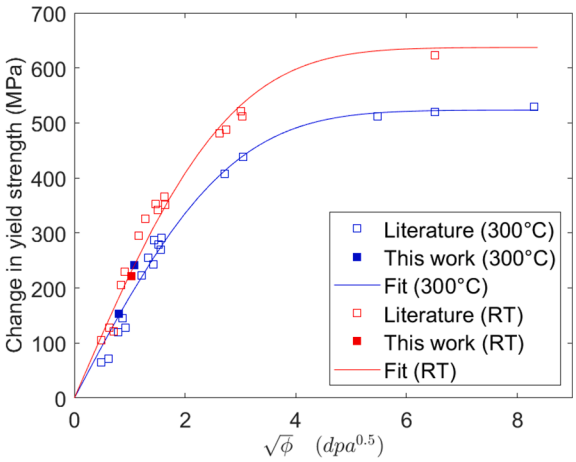

Fig. 5. Results of curve fitting parameters a, $\sqrt{N_s}$ and h_N at RT and 300 °C with data from experiments and from literature [22,51,52].

Table 3
List of viscoplastic GTN ductile damage model parameters. Parameters marked with * are taken from literature [12,27,34].

T (°C)	q_1	q_2	ϵ_N	s_N	f_N	f_c	$f_{c,irr}$	f_F
RT	1.5*	1.0*	0.3*	0.1*	0.0018	0.0045*	0.00243	0.1*
300	1.5*	1.0*	0.3*	0.1*	0.0013	0.0045*	0.00206	0.1*

Table 4
List of irradiation defect density evolution parameters identified in this work.

T (°C)	n_{irr} (MPa)	a	h_N	$\sqrt{N_s}$ (MPa)	b	$l_{N,0}$	$l_{N,1}$	N_e
RT	3.62	0.1326	1.2165	526	47.98	0.855	0.42	1.0
300	3.03	0.1326	1.0	526	78.19	0.562	0.18	1.5

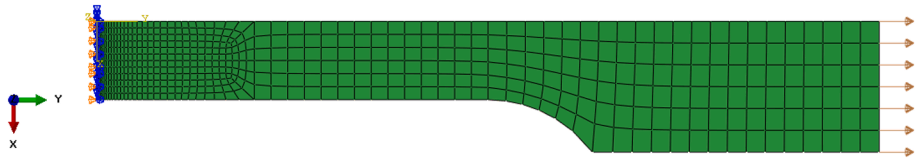

Fig. 6. Axisymmetric model of tensile specimen with boundary conditions.

imposed via velocity boundary conditions. For irradiated specimens, irradiation and tension load are simulated sequentially. The state variables discussed are extracted from the first element to fail.

5.1. Mesh convergence

The characteristic element width $a = d_0/12$ was used with systematic refinement (a, $a/2$, $a/4$). While meshes with initial aspect ratio AR (= width/height) ≈ 1 showed convergence of the engineering curve at $a/4$, local quantities remained scattered due to severe element thinning in the neck leading to large element aspect ratios at coalescence. Fixing the element width at $a/2$, the initial AR is varied (1 to 8) in the neck region, identifying an optimal initial AR ≈ 5, for which the AR at coalescence ($p \approx 1.34$) is close to unity, and both total strain and neck radius converged as seen in Fig. 7. Therefore, the element size of 0.1 × 0.02 mm is adopted in the gauge section, with the smaller dimension remaining larger than the mean void diameter of 3–9 μm reported by Stratil [55].

5.2. Experimental validation

From simulations performed under all testing conditions, the engineering stress–strain ($\sigma_{eng} - \epsilon_{eng}$) and mean true stress–strain ($\sigma_T - \epsilon_T$) responses are extracted and compared with experimental data. Results from the unirradiated and irradiated (0.65 dpa) specimens tested at $\dot{u} = 0.2$ mm/min show very good agreement in Fig. 8, demonstrating the model's capability to accurately describe the material's strain hardening and fracture strain in both unirradiated and irradiated states. Agreement in mean true strain indicates a good description of the necking behavior and the reduction in the minimum cross-section.

In Fig. 9a, the simulated profile of unirradiated specimen at failure is superimposed over the corresponding experimental image and

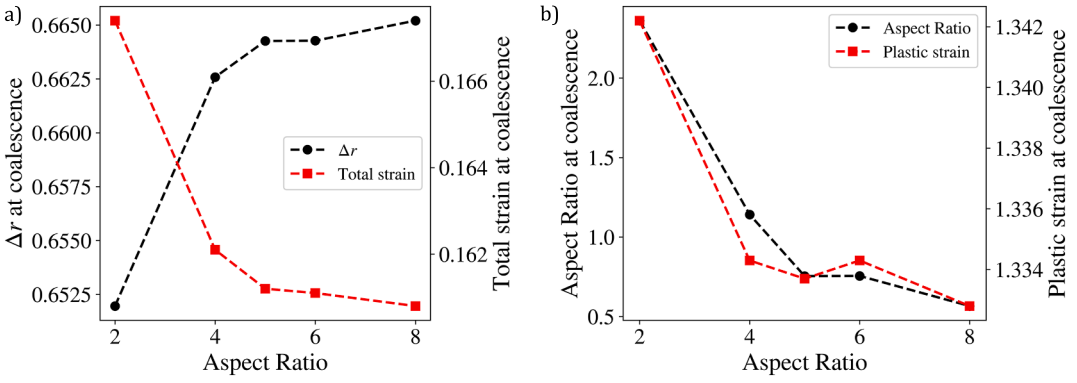

Fig. 7. Mesh-convergence study for varying initial aspect ratios: (a) global response metrics and (b) quantities extracted from the damaged element.

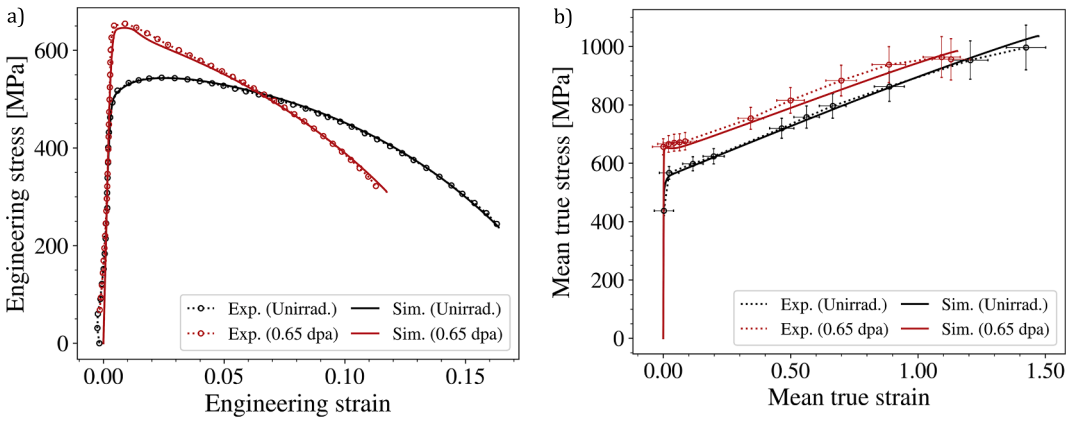

Fig. 8. Comparison of simulated and experimental results from tensile tests of unirradiated and irradiated specimens at $T_{test} = 300\ ^{\circ}C$ and $\dot{u} = 0.2$ mm/min using a) engineering stress–strain and b) mean true stress–strain plots with error bars.

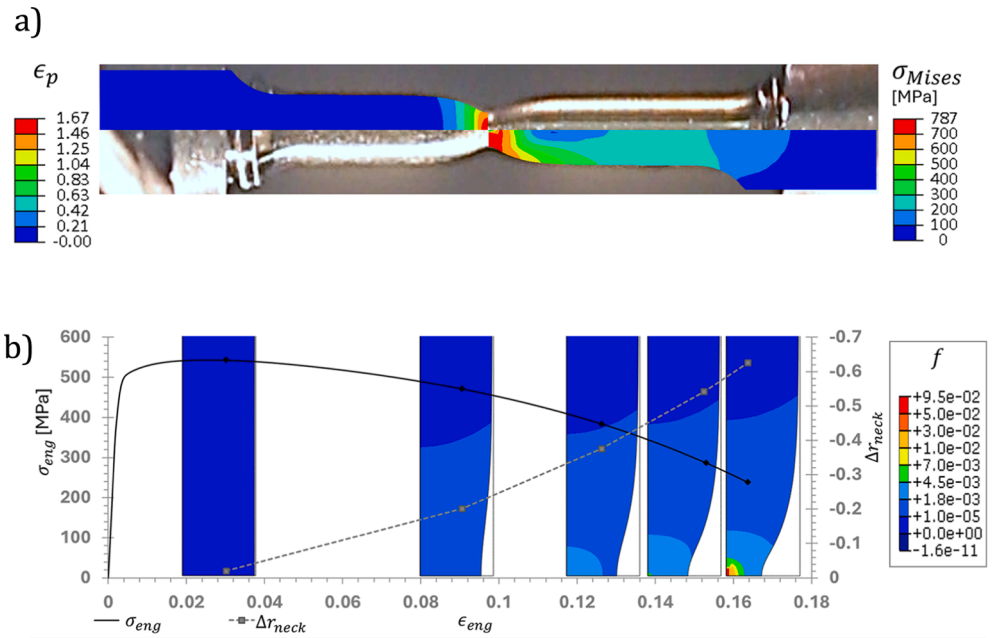

Fig. 9. Deformation and ductile damage of unirradiated specimen at $T_{test} = 300\ ^{\circ}C$: a) comparison of experimental and simulated specimen profiles at failure, highlighting accumulated plastic strain (p) and von-Mises stress (σ_{Mises}) distributions, and b) evolution of void volume fraction (f) and reduction of neck radius (Δr_{neck}) relative to engineering stress (σ_{eng}) and strain ($\in_{eng}$).

shows good agreement. Stress and plastic deformation localize at the neck, leading to ductile damage development, which is illustrated in Fig. 9b through the evolution of VVF. The evolution of VVF relative to the change in minimum radius at the neck (Δr_{neck}) compared with the engineering stress–strain highlights the influence of triaxiality on ductile damage. A similar comparison for the irradiated

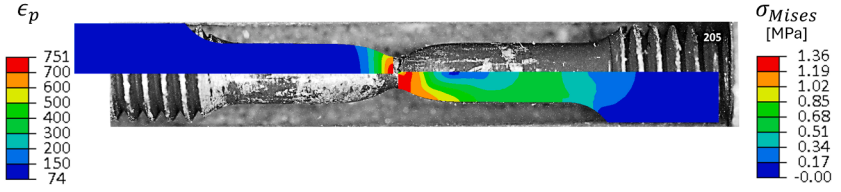

Fig. 10. Comparison of experimental and simulated specimen profiles at failure, highlighting accumulated plastic strain (p) and irradiation hardening (σ_H) distributions.

Table 5
Comparison of predicted and experimental $\sigma_{eng.\,UTS}$ and $\in_{eng.\,fr}$ for unirradiated and irradiated Eurofer97 under different loading conditions.

T_{test}(°C)	$\dot{u}$ (mm/min)	Dose (dpa)	$\sigma_{eng.\,UTS}$	$\Delta\sigma_{eng.\,UTS}$ (%)	$\in_{eng.\,fr}$	$\Delta\in_{eng.\,fr}$(%)
RT	0.2	0	710.3	0.37	0.1999	−0.47
RT	0.2	1.05	826.0	−4.19	0.1287	7.92
RT	0.2	70	1210.2	−0.49	0.1236	−1.97
RT	2.0	0	722.9	−0.08	0.2074	2.46
100	2.0	0	662.6	4.71	0.1943	−1.14
200	2.0	0	600.8	2.21	0.1806	−2.94
300	2.0	0	546.4	1.91	0.1659	−2.85
300	0.2	0	543.0	−0.39	0.1638	0.49
300	0.2	0.65	645.8	−1.52	0.1173	3.99
300	0.2	1.18	689.0	−7.41	0.1083	2.62
300	0.2	70	970.7	0.01	0.1175	4.97

specimen in Fig. 10 shows that the reduction in minimum radius is slightly underestimated. The superposed contour plots illustrate the reduction in irradiation hardening σ_H in regions of strong plastic deformation.

The predicted values of σ_{eng} at loss of uniform elongation $\sigma_{eng.\,UTS}$ and the $\in_{eng}$ at failure, $\in_{eng.\,fr}$, and their deviation from experimental values are compared in Table 5, with results at $T_{test} = 100$ and 200 °C included as blind predictions. For unirradiated specimens, the scatter in $\sigma_{eng.\,UTS}$ remains below 5%, while deviations in $\in_{eng.\,fr}$ are within 3%. $\in_{eng.\,fr}$ is seen to increase at higher $\dot{u}$. Larger scatter is observed at the lower irradiation doses, whereas the agreement at high dose is generally good. Underestimation of σ_H, leading to lower $\sigma_{eng.UTS}$ results in an overestimation in $\in_{eng.fr}$. Results at 100 and 200 °C, demonstrate good predictive accuracy, with mostly conservative deviations. The comparison of other results is shown in Fig. 11. Overall, the results demonstrate good predictive accuracy of the model within the investigated temperature and irradiation range.

To demonstrate the model's cyclic capability enabled by the kinematic hardening, simulation of strain-controlled loads with strain range $\Delta\in = 1.0\%$ at 300 °C were simulated for unirradiated and irradiated (2.5 dpa@T_{irr} = 300 °C) conditions. The predicted cyclic response is compared with experimental data [56] in Fig. 12 shows generally good agreement, although the yield stress of the

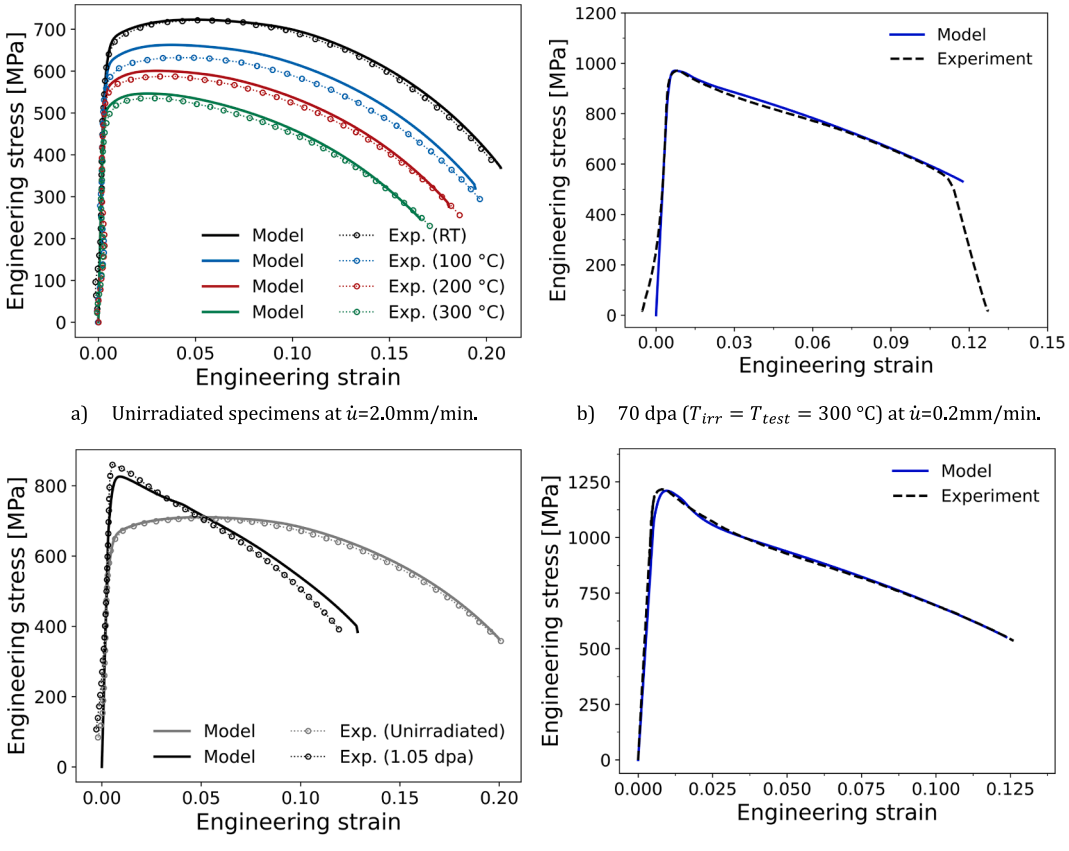

a) Unirradiated specimens at $\dot{u}$=2.0mm/min.

b) 70 dpa ($T_{irr} = T_{test} = 300$ °C) at $\dot{u}$=0.2mm/min.

c) $T_{test} = RT$ ($T_{irr} = 300$ °C).

d) 70 dpa ($T_{irr} = 300$ °C, $T_{test} = RT$).

Fig. 11. Comparison of predicted and experimental tensile test results of unirradiated and irradiated specimens.

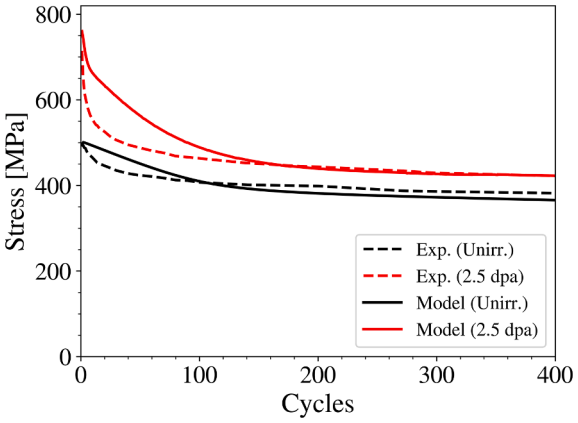

Fig. 12. Comparison of predicted and experimental low cycle fatigue results [56] of unirradiated and irradiated specimens (2.5 dpa) for 1.0% strain range at $T_{test} = 300\ ^{\circ}C$ and $T_{irr} = 300\ ^{\circ}C$.

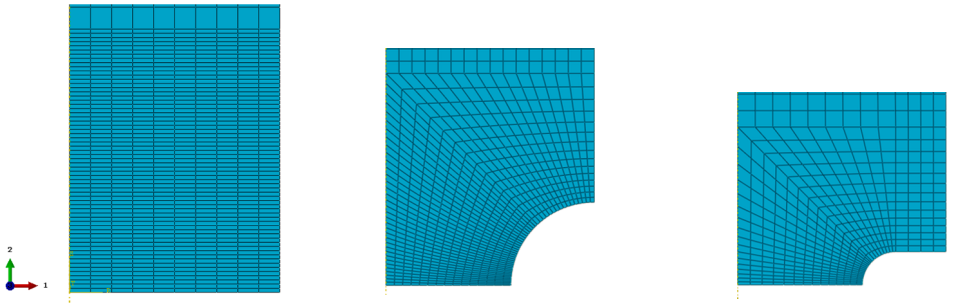

(a) smooth specimen (b) notch radius 0.5 mm (c) notch radius 0.2 mm

Fig. 13. Meshing near the symmetry plane in axisymmetric models of smooth and notched tensile specimens.

simulated irradiated specimen is overestimated.

5.3. Ductility study on smooth and notched specimens

Next, the model is applied to different irradiation doses and initial triaxialities to study the predicted reduction in ductility at $T_{irr} = T_{test} = 300\ ^{\circ}C$. Geometries of smooth and notched specimen from [57] are used, where the gauge section is of 2 mm diameter and 5 mm length. The notched specimens have notch radii of 0.5 and 0.2 mm, and an inner diameter of 1.5 mm. Axisymmetric models are setup following the same approach from section 5.1. In regions closest to the symmetry plane (XY) where necking and failure is expected, finer mesh with element of AR = 5 is used to limit element thinning as shown in Fig. 13. As the predicted σ_H saturates at 43.25 dpa, a set of thirteen doses between 0–43.25 dpa are selected to achieve an even distribution of irradiation hardening.

The engineering curves of smooth specimens in Fig. 14a show that for increasing levels of irradiation dose, the model can consistently describe the increase of material hardening. The rate of necking at the minimum cross-section is aggravated by the increase in dose as seen in Fig. 14b, which leads to increasingly steeper post-yield relaxation. Ultimately the tensile ductility also reduces, evident from the reduction in engineering fracture strain. Key metrics from the simulation results are summarized in Fig. 14c, which indicate that σ_H increases with dose initially and saturates beyond ~10 dpa. While the strain at uniform elongation completely vanishes for doses < 0.7 dpa, the strain at total elongation reduces drastically till ~10 dpa. Beyond 10 dpa, these metrics are seen to stabilize and saturate, which is in good agreement with the findings of [6]. The reduction in minimum area Z follows a trend similar to total elongation. As total elongation and Z are measures of material ductility, the model is effectively shown to be capable of describing the irradiation induced reduction in ductility.

The predicted load–displacement data extracted from simulations performed on the two notched specimens are plotted in Fig. 15. Due to the higher initial triaxiality of notch radius 0.2 mm in comparison to 0.5 mm, the peak load is larger, while the total elongation and the fracture strain are lower. The irradiation-induced changes in material properties, such as material hardening and the reduction in ductility, are consistent with the results seen in the smooth specimen. The notched specimen results are presented as model predictions to assess the effect of stress triaxiality, rather than as direct experimental validations.

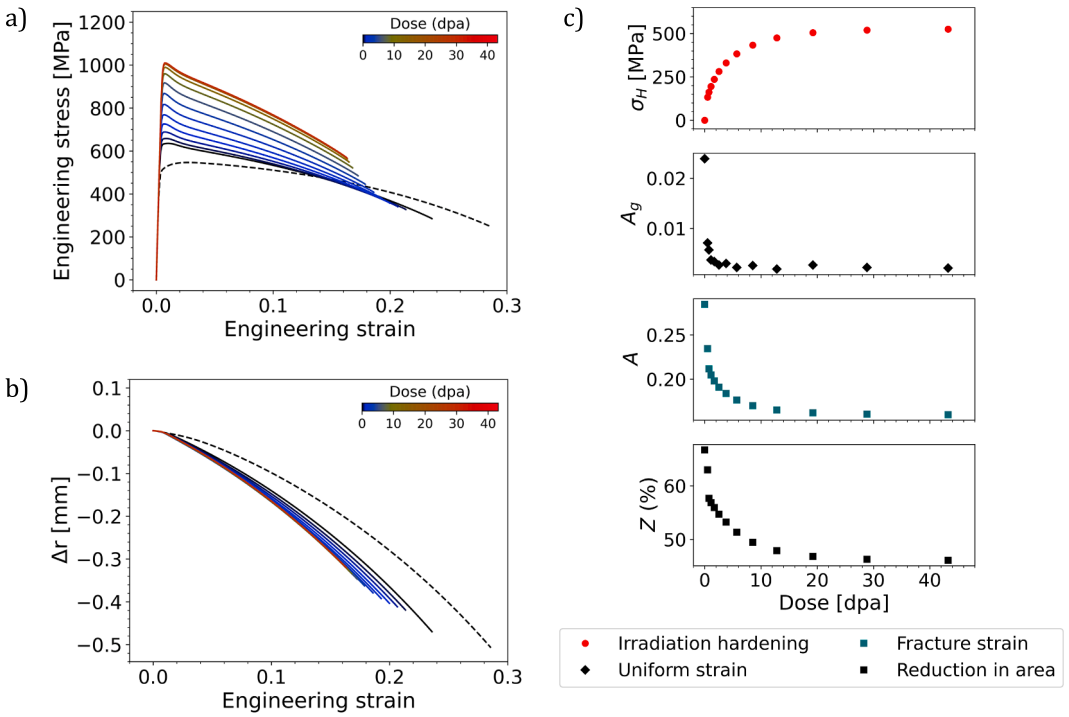

Fig. 14. Simulated irradiation influence on a) engineering stress–strain, b) reduction of neck radius, and c) general tensile properties of smooth specimen at 300 °C.

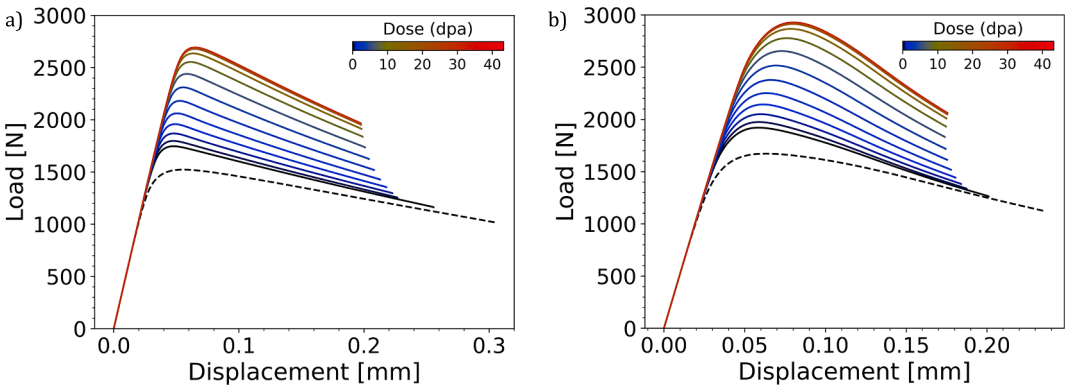

Fig. 15. Simulated load displacement curves of specimens with notch radius a) 0.5 mm and b) 0.2 mm at 300 °C.

6. Discussion

From the simulations performed using the smooth specimen, data were extracted from the first element to fail in each case, which is consistently located at the center of the neck region. The evolution of several key variables is plotted against the accumulated plastic strain p, to discuss the predicted deformation and ductile damage behavior.

The true stress (S) plotted in Fig. 16a indicates that hardening in unirradiated material is nearly linear, characterized by a positive hardening modulus (HM) given by dS/dA. Increase in irradiation dose delivers an increase in yield stress. Post yield, irradiated specimens display a steep drop in stress initially, but this is stabilized due to strain hardening governed by the kinematic hardening model.

At higher irradiation doses, where the defect density is larger, the defect removal under plastic deformation induces more significant material softening. This is quantified through the evolution of σ_H in Fig. 16b, where a rapid reduction is observed at the onset of plasticity, followed by stabilization and a steady rate of further reduction. The stabilization is controlled by parameter l_N. At a microstructure level, this indicates that the established deformation mechanism of channeling in irradiated materials [4,22] may not be sustained at a constant rate. The large strain energy available at yielding due to increased yield stress is likely sufficient only for a

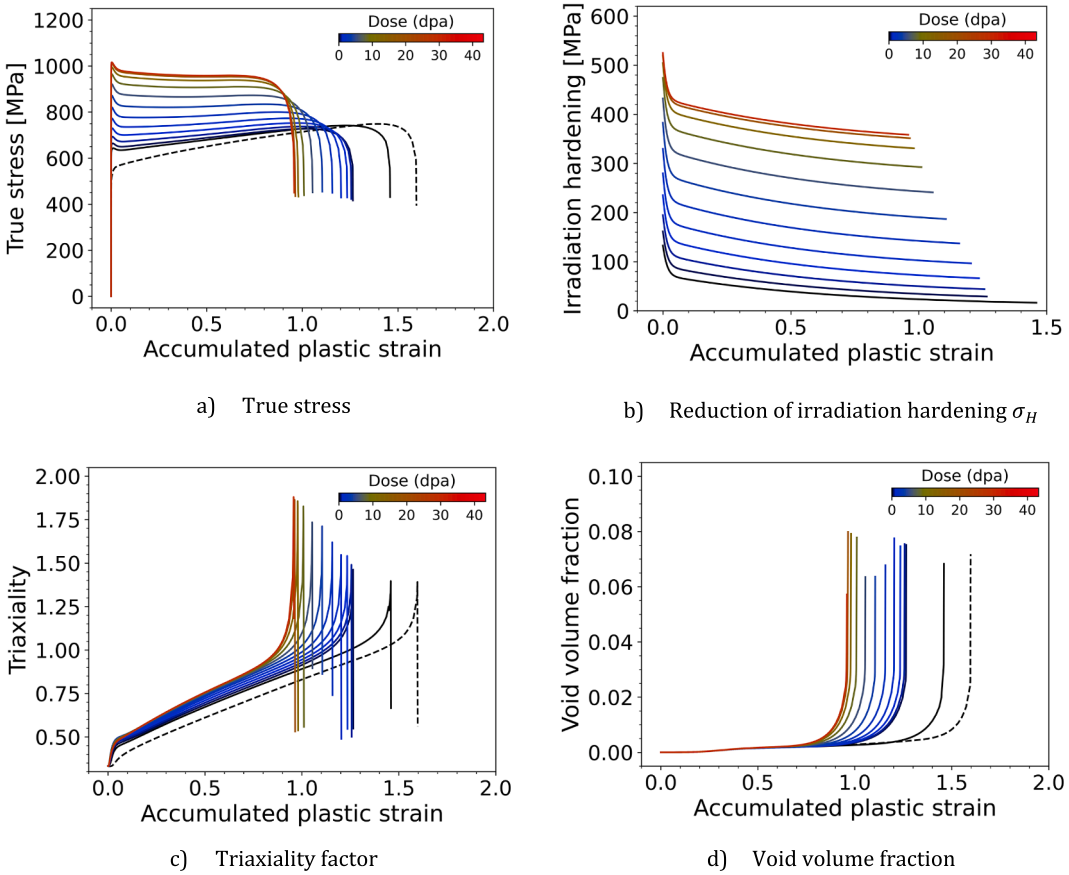

a) True stress

b) Reduction of irradiation hardening σ_H

c) Triaxiality factor

d) Void volume fraction

Fig. 16. Irradiation influence on true stress and several other metrics plotted against accumulated plastic strain.

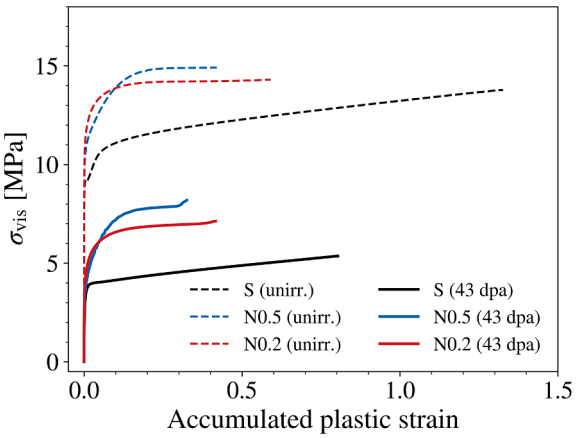

Fig. 17. Comparison of simulated σ_{vis} in smooth (S) and notched specimens of radius 0.5 mm (N0.5) and 0.2 mm (N0.2) for unirradiated and irradiated (43 dpa) materials simulated at 300 °C.

temporary high rate of dislocation nucleation and defect removal. As studies on such stabilization have not been reported in literature, it remains a prediction made based on the simulations performed in this work. The simulations also indicate that a significant portion of the initially nucleated defects remain at failure, especially at higher doses.

Reduction in σ_H directly leads to a decrease in HM, which explains the plateauing of the true stress curves with increasing dose. This irradiation-dependent reduction of HM promotes earlier plastic instability, as lower hardening capacity favors localization and neck development [58]. The stress triaxiality factor shown in Fig. 16c, computed as S_v/S_{eq} from the Cauchy stress tensor, reflects this

instability behavior. Accelerated necking produces a more rapid increase in stress triaxiality, which in combination with the identified $f_{c,irr}$ results in an accelerated void growth and coalescence as shown in Fig. 16d. Consequently, the predicted plastic fracture strain reduces with increase in dose. Stress triaxiality consistently peaks in all simulated conditions and subsequently falls due to a drop in von-Mises stress and hydrostatic stress, signaling the loss of load bearing capacity and material.

As shown in Fig. 17, σ_{vis} increases rapidly in the necking region due to strong strain localization, where local strain rates significantly exceed the global rate despite quasi static loading. The lower magnitude of σ_{vis} in the irradiated material is consistent with the reduced rate sensitivity in irradiated RAFM steels [39]. Consequently, the formulation captures the accelerated localization and earlier neck development in the irradiated condition, while the higher rate sensitivity of the unirradiated material leads to a more gradual localization.

From a numerical standpoint, the viscoplastic formulation regularizes strain localization and significantly mitigates mesh sensitivity in the post-necking regime [32,33]. However, element distortion in the neck region due to large strains can lead to overestimation of reduction in minimum area [59]. As discussed in section 5.1, this effect is addressed by employing elements of sufficiently high aspect ratio oriented perpendicular to the loading axis. This ensure that the element's aspect ratio is closer to unity at the onset of void coalescence, thereby improving the accuracy of localization and failure predictions [59].

Since the model is formulated in terms of stress invariants, it is applicable to general multiaxial stress states. The classical GTN model was developed for monotonic loading and is known to exhibit limitations in shear-dominated conditions. The inclusion of kinematic hardening and viscoplastic regularization allows application to non-proportional and cyclic loading and rate-dependent loading. However, the GTN framework does not explicitly represent fatigue damage mechanisms. Therefore, the presented validation focuses on high stress triaxiality conditions (TF $>$ 0.33), which govern void-controlled ductile damage in Eurofer97 and are most relevant for structural safety assessments.

Implicit integration based on backward Euler return mapping is unconditionally stable, but requires derivation of the model Jacobian which is significantly complex for the developed model. Furthermore, implicit schemes are known to encounter convergence issues near void-coalescence, where material softening becomes prominent [60]. Explicit schemes are simple to implement; but for viscoplastic models of consistency-type their primary limitation is enforcement of consistency condition. The explicit scheme adopted in this work circumvents this by computing the σ_{vis} through a scalar root-finding operation, thereby decoupling the consistency enforcement from the integration. The resulting algorithm remains robust even during material failure. However, the conditional stability of the explicit scheme restricts admissible time step size and would increase the total computational time relative to the implicit methods.

7. Conclusion

A viscoplastic extension of the Gurson-Tvergaard-Needleman ductile damage model for a strain hardening material is proposed in this work, incorporating several ideas such as hydrostatic and deviatoric flow stress and limiting surface from other authors. Strain hardening of the material is described by the Chaboche-type kinematic hardening and isotropic softening laws incorporated by an existing finite strain viscoplastic model, where irradiation influence on material properties is described through the evolution of irradiation defect density.

Considering that the strain rate sensitivity is solely contributed by the matrix material and the viscoplasticity framework, this work proposes a simple method to determine the viscous stress using the consistency conditions of the viscoplastic GTN yield criterion. An analytical flow rule for the viscoplastic GTN model and plastic multiplier is also derived. The derived model is implemented in a commercial FE program and calibrated at RT and 300 °C using available load–displacement data from experiments and literature. Model validations confirm the model's ability to accurately describe the deformation and ductile damage of unirradiated and irradiated material. Irradiation influence and the role of triaxiality are investigated with simulations on smooth and notched tensile specimens subjected to a wide range of irradiation doses, which confirm that the model results are consistent and irradiation-influenced changes in material properties are rampant only at low doses, with stabilization occurring around 10 dpa. The model is a reliable tool for assessing the plastic flow localization and safe limits of fusion reactor components.

CRediT authorship contribution statement

Roshan R. Rajakrishnan: Writing – original draft, Software, Methodology, Conceptualization. **Ermile Gaganidze:** Writing – review & editing, Funding acquisition, Conceptualization. **Jarir Aktaa:** Writing – review & editing, Methodology, Conceptualization.

Funding

This project has received funding from the KIT Fusion program and the Euratom research and training program 2014–2018 under grant agreement No 755039 (M4F Project).

Declaration of competing interest

The authors declare that they have no known competing financial interests or personal relationships that could have appeared to influence the work reported in this paper.

Data availability

The authors do not have permission to share data.

References

[1] Van Der Schaaf B, Gelles DS, Jitsukawa S, Kimura A, Klueh RL, Möslang A, et al. Progress and critical issues of reduced activation ferritic/martensitic steel development. J Nucl Mater 2000;283–287:52–9. https://doi.org/10.1016/S0022-3115(00)00220-8.
[2] Lucon E, Decréton M, Van Walle E. Mechanical characterization of EUROFER97 irradiated (0.32 dpa, 300°C). Fusion Engng Des 2003;69:373–7. https://doi.org/10.1016/S0920-3796(03)00075-9.
[3] Dethloff C, Gaganidze E, Aktaa J. Microstructural defects in EUROFER 97 after different neutron irradiation conditions. Nucl Mater Energy 2016;9:471–5. https://doi.org/10.1016/j.nme.2016.05.009.
[4] Chaouadi R. Effect of irradiation-induced plastic flow localization on ductile crack resistance behavior of a 9%Cr tempered martensitic steel. J Nucl Mater 2008;372:379–90. https://doi.org/10.1016/j.jnucmat.2007.04.044.
[5] Wang K, Dai Y, Spätig P. Microstructure and fracture behavior of F82H steel under different irradiation and tensile test conditions. J Nucl Mater 2016;468:246–54. https://doi.org/10.1016/j.jnucmat.2015.09.031.
[6] Gaganidze E, Petersen C, Materna-Morris E, Dethloff C, Weiß OJ, Aktaa J, et al. Mechanical properties and TEM examination of RAFM steels irradiated up to 70dpa in BOR-60. J Nucl Mater 2011;417:93–8. https://doi.org/10.1016/j.jnucmat.2010.12.047.
[7] Noell P, Carroll J, Hattar K, Clark B, Boyce B. Do voids nucleate at grain boundaries during ductile rupture? Acta Mater 2017;137:103–14. https://doi.org/10.1016/j.actamat.2017.07.004.
[8] Was GS. Fundamentals of radiation materials science: metals and alloys. Berlin; New York: Springer; 2007.
[9] Ling C, Tanguy B, Besson J, Forest S, Latourte F. Void growth and coalescence in triaxial stress fields in irradiated FCC single crystals. J Nucl Mater 2017;492:157–70. https://doi.org/10.1016/j.jnucmat.2017.04.013.
[10] Patra A, McDowell DL. A void nucleation and growth based damage framework to model failure initiation ahead of a sharp notch in irradiated bcc materials. J Mech Phys Solids 2015;74:111–35. https://doi.org/10.1016/j.jmps.2014.10.006.
[11] Aiello G, Aktaa J, Cismondi F, Rampal G, Salavy J-F, Tavassoli F. Assessment of design limits and criteria requirements for Eurofer structures in TBM components. J Nucl Mater 2011;414:53–68. https://doi.org/10.1016/j.jnucmat.2011.05.005.
[12] Stratil L, Siska F, Hadraba H, Dlouhy I. Modeling of ductile tearing for RAFM steel eurofer97. Procedia Mater Sci 2014;3:1155–60. https://doi.org/10.1016/j.mspro.2014.06.188.
[13] Tvergaard V. Influence of voids on shear band instabilities under plane strain conditions. Int J Fract 1981;17:389–407. https://doi.org/10.1007/BF00036191.
[14] Tvergaard V. Material failure by void coalescence in localized shear bands. Int J Solids Struct 1982;18:659–72. https://doi.org/10.1016/0020-7683(82)90046-4.
[15] Chakraborty P, Biner SB. Parametric study of irradiation effects on the ductile damage and flow stress behavior in ferritic-martensitic steels. J Nucl Mater 2015;465:89–96. https://doi.org/10.1016/j.jnucmat.2015.05.054.
[16] Becker R, Needleman A, Richmond O, Tvergaard V. Void growth and failure in notched bars. J Mech Phys Solids 1988;36:317–51. https://doi.org/10.1016/0022-5096(88)90014-2.
[17] Hao S, Brocks W. The Gurson-Tvergaard-Needleman-model for rate and temperature-dependent materials with isotropic and kinematic hardening. Comput Mech 1997;20:34–40. https://doi.org/10.1007/s004660050213.
[18] Vadillo G, Zaera R, Fernández-Sáez J. Consistent integration of the constitutive equations of Gurson materials under adiabatic conditions. Comput Methods Appl Mech Engng 2008;197:1280–95. https://doi.org/10.1016/j.cma.2007.11.008.
[19] Wang WM, Sluys LJ, De Borst R. Viscoplasticity for instabilities due to strain softening and strain-rate softening. Int J Numer Meth Engng 1997;40:3839–64. https://doi.org/10.1002/(SICI)1097-0207(19971030)40:20%253C3839::AID-NME245%253E3.0.CO;2-6.
[20] Klingbeil D, Svendsen B, Reusch F. Gurson-based modelling of ductile damage and failure during cyclic loading processes at large deformation. Engng Fract Mech 2016;160:95–123. https://doi.org/10.1016/j.engfracmech.2016.03.023.
[21] Aktaa J, Petersen C. Modeling the influence of high dose irradiation on the deformation and damage behavior of RAFM steels under low cycle fatigue conditions. J Nucl Mater 2009;389:432–5. https://doi.org/10.1016/j.jnucmat.2009.02.032.
[22] Rajakrishnan RR, Gaganidze E, Terentyev D, Aktaa J. Macro-scale modeling of finite strain viscoplasticity in irradiated F/M steels: a continuum thermodynamic framework. Contin Mech Thermodyn 2023;35:521–43. https://doi.org/10.1007/s00161-023-01193-0.
[23] Jansohn W. Formulierung und Integration von Stoffgesetzen zur Beschreibung großer Deformationen in der Thermoplastizität und -Viskoplastizität. 1997.
[24] Haupt P. Continuum Mechanics and Theory of Materials. Berlin, Heidelberg: Springer Berlin Heidelberg; 2002. doi:10.1007/978-3-662-04775-0.
[25] Truesdell C, Noll W, Antman SS. The non-linear field theories of mechanics. 3. ed. Berlin Heidelberg: Springer; 2004.
[26] Gurson AL. Continuum theory of ductile rupture by void nucleation and growth. Part I. In: Yield criteria and flow rules for porous ductile media; 1975. https://doi.org/10.2172/7351470.
[27] Tvergaard V, Needleman A. Analysis of the cup-cone fracture in a round tensile bar. Acta Metall 1984;32:157–69. https://doi.org/10.1016/0001-6160(84)90213-X.
[28] Mear ME, Hutchinson JW. Influence of yield surface curvature on flow localization in dilatant plasticity. Mech Mater 1985;4:395–407. https://doi.org/10.1016/0167-6636(85)90035-3.
[29] Leblond J-B, Perrin G, Devaux J. An improved Gurson-type model for hardenable ductile metals. Eur J Mech -Solids 1995;14:499–527.
[30] Devaux J, Gologanu M, Leblond JB, Perrin G. On Continued Void Growth in Ductile Metals Subjected to Cyclic Loadings. In: Willis JR, editor. IUTAM Symp. Nonlinear Anal. Fract., vol. 49, Dordrecht: Springer Netherlands; 1997, p. 299–310. doi:10.1007/978-94-011-5642-4_28.
[31] Pascon JP, Waisman H. A thermodynamic framework to predict ductile damage in thermoviscoplastic porous metals. Mech Mater 2021;153:103701. https://doi.org/10.1016/j.mechmat.2020.103701.
[32] Needleman A. Material rate dependence and mesh sensitivity in localization problems. Comput Methods Appl Mech Engng 1988;67:69–85. https://doi.org/10.1016/0045-7825(88)90069-2.
[33] Pan J, Saje M, Needleman A. Localization of deformation in rate sensitive porous plastic solids. Int J Fract 1983;21:261–78. https://doi.org/10.1007/BF00942345.
[34] Chu CC, Needleman A. Void Nucleation Effects in Biaxially Stretched Sheets. J Engng Mater Technol 1980;102:249–56. https://doi.org/10.1115/1.3224807.
[35] Needleman A, Tvergaard V. An analysis of dynamic, ductile crack growth in a double edge cracked specimen. Int J Fract 1991;49:41–67. https://doi.org/10.1007/BF00013502.
[36] Aktaa J, Petersen C. Modeling the constitutive behavior of RAFM steels under irradiation conditions. J Nucl Mater 2011;417:1123–6. https://doi.org/10.1016/j.jnucmat.2010.12.295.
[37] Chaboche JL. Constitutive equations for cyclic plasticity and cyclic viscoplasticity. Int J Plast 1989;5:247–302. https://doi.org/10.1016/0749-6419(89)90015-6.
[38] Byun T, Hashimoto N. Strain localization in irradiated materials. Nucl Engng Technol 2006.
[39] Hashimoto N, Zinkle SJ, Klueh RL, Rowcliffe AF, Shiba K. Deformation Mechanisms in Ferritic/martensitic Steels Irradiated in HFIR. MRS Proc 2000;650:R1.10. doi:10.1557/PROC-650-R1.10.
[40] Abaqus User Subroutines Reference Guide n.d.

[41] Hughes TJR, Winget J. Finite rotation effects in numerical integration of rate constitutive equations arising in large-deformation analysis. Int J Numer Meth Engng 1980;15:1862–7. https://doi.org/10.1002/nme.1620151210.
[42] Weber GG, Lush AM, Zavaliangos A, Anand L. An objective time-integration procedure for isotropic rate-independent and rate-dependent elastic-plastic constitutive equations. Int J Plast 1990;6:701–44. https://doi.org/10.1016/0749-6419(90)90040-L.
[43] Fehlberg E. Low-order classical Runge-Kutta formulas with stepsize control and their application to some heat transfer problems. NASA 1969.
[44] Richard P. Brent. Algorithms for Minimization without Derivatives. New Jersey: Prentice-Hall; n.d.
[45] Fleig T. Lebensdaueranalyse unter Berücksichtigung viskoplasticher Verformung und Schädigung mit der Methode der Finite Elemente. Universität Karlsruhe 1996.
[46] Bond WL. The Mathematics of the Physical Properties of Crystals. Bell Syst Tech J 1943;22:1–72. https://doi.org/10.1002/j.1538-7305.1943.tb01304.x.
[47] Ting, T. C. T. Anisotropic Elasticity. Theory and Applications. New York: Oxford University Press; 1996. doi:10.1002/zamm.19970770617.
[48] Dmitry Terentyev, SCK-CEN. Personal communication 2020.
[49] Lucon E, Benoit P, Jacquet P, Diegele E, Lässer R, Alamo A, et al. The European effort towards the development of a demo structural material: Irradiation behaviour of the European reference RAFM steel EUROFER. Fusion Eng Des 2006;81:917–23. doi:10.1016/j.fusengdes.2005.08.044.
[50] Whapham AD, Makin MJ. The hardening of lithium fluoride by electron irradiation. Phil Mag 1960;5:237–50. https://doi.org/10.1080/14786436008235839.
[51] Gaganidze E, Claus Petersen. Post irradiation examination of RAF/M steels after fast reactor irradiation up to 71 dpa and < 340°C (ARBOR 2) : RAFM Steels: Metallurgical and Mechanical Characterisation. (KIT Scientific Reports ; 7596). Karlsruher Institut für Technologie (KIT); 2011.
[52] Petersen C. Post irradiation examination of RAF/M steels after fast reactor irradiation up to 33 dpa and < 340 °C (ARBOR 1). Forschungszentrum Karlsruhe GmbH Technik und Umwelt (Germany); 2010.
[53] Knitel S, Spätig P, Yamamoto T, Seifert HP, Dai Y, Odette GR. Evolution of the tensile properties of the tempered martensitic steel Eurofer97 after spallation irradiation at SINQ. Nucl Mater Energy 2018;17:69–77. https://doi.org/10.1016/j.nme.2018.09.002.
[54] Lucon E, Leenaers A, Vandermeulen W. Post-irradiation mechanical properties of three EUROFER97 joints. Fusion Engng Des 2008;83:620–4. https://doi.org/10.1016/j.fusengdes.2008.01.008.
[55] Stratil L, Hadraba H, Dlouhý I. Ductile damage identification and tensile notch effect for EUROFER97 steel. Acta Metall Slovaca - Conf 2013;3:185–90. https://doi.org/10.12776/amsc.v3i0.125.
[56] Luzginova NV, Rensman J, Ten Pierick P, Hegeman JBJ. Low cycle fatigue of irradiated and unirradiated Eurofer97 steel at 300°C. J Nucl Mater 2011;409:153–5. https://doi.org/10.1016/j.jnucmat.2010.09.017.
[57] Mahler M, Fessi S, Aktaa J. Simplified approach for ductile fracture mechanics SSTT and its application to Eurofer97. Nucl Mater Energy 2021;26:100799. https://doi.org/10.1016/j.nme.2020.100799.
[58] Considère M. Mèmoire sur l'emploi du fer et de l'acier dans les constructions. Vue Ch: Dunod; 1885.
[59] Xue Z, Pontin MG, Zok FW, Hutchinson JW. Calibration procedures for a computational model of ductile fracture. Engng Fract Mech 2010;77:492–509. https://doi.org/10.1016/j.engfracmech.2009.10.007.
[60] Simo JC, Hughes TJR. Computational inelasticity. New York: Springer; 1998.